ACS APPLIED POLYMER MATERIALS

pubs.acs.org/acsapm

Article

Three-Dimensional Printing of Liquid Crystals with Thermal Sensing Capability via Multimaterial Vat Photopolymerization

Dylan Joralmon, Saleh Alfarhan, Stephanie Kim, Tengteng Tang, Kailong Jin,* and Xiangjia Li*

Cite This: *ACS Appl. Polym. Mater.* 2022, 4, 2951−2959

Read Online

ACCESS | Metrics & More | Article Recommendations | Supporting Information

ABSTRACT: Creatures in nature possess unique smart material systems that can sense environmental changes with evolved self-responsible architectures. For example, the *Japetella heathi* octopus exhibits a remarkable ability to change its appearance to evade the attention of predators. Here, we present an approach to produce *Japetella heathi*-inspired smart materials with thermal sensing architectures by multimaterial three-dimensional (3D) printing, where both conventional acrylic-based ultraviolet resins and reactive liquid crystals (LCs) are photocured to form an object with desired patterns. The levels of orientational and positional orders of LCs in unique thermodynamic phases (e.g., nematic and isotropic phases) can be modulated by the local temperature of the material. As a result, the 3D printed liquid crystalline materials (within the printed multimaterial object) possess a unique optical property that can reversibly transition from opaque (in the nematic phase) to transparent (in the isotropic phase) in response to external thermal stimuli. The multimaterial 3D printing process provides a versatile manufacturing tool that enables the design and fabrication of bioinspired smart materials with complex 3D shapes for various potential applications, such as soft robots, flexible sensors, and smart anticounterfeiting devices.

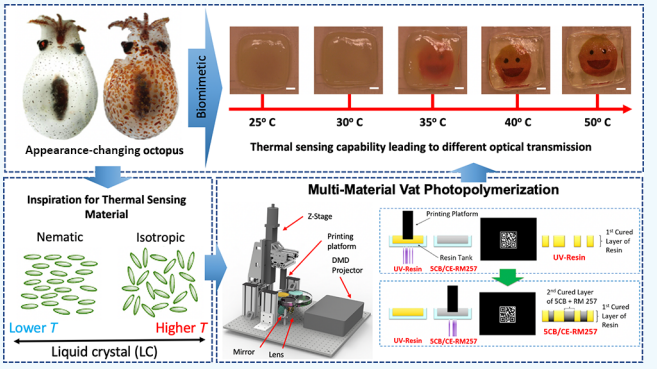

KEYWORDS: *3D printing, vat photopolymerization, liquid crystal, multimaterial, temperature sensor*

1. INTRODUCTION

Over the span of millions of years, creatures have evolved to create a multitude of complex materials and structures that possess superior physical properties.[1] Biological constructs have been optimized for a broad range of functional requirements such as gathering food using mechanically reinforced appendages,[2] signaling,[3] and evading predators using camouflage[4] through minuscule changes in the surrounding environment. Consequently, naturally occurring structures and biological materials provide a rich source of inspiration for the design of next-generation multifunctional devices with bioinspired architectures due to the remarkable properties exhibited by different organisms. For example, self-responsive architectures in the *Japetella heathi* octopus exhibit the ability to reversibly change its appearance from totally transparent to partially opaque in order to evade predators (Figure 1a).[5] Moreover, different external stimuli have been shown to influence optical properties in the cuticles of the Hercules beetle, leading to alterations in nanoporous structures for the development of self-sensors in response to humidity levels in the environment.[6] These microstructures are typically colloidal multimaterial systems that can show dynamic structural colors depending on the arrangement and orientation of biological materials, which in turn determine their refractive indices and light scattering effects.[7]

Therefore, the exemplary optical appearance change mechanisms from nature provide a promising design template for the development of smart materials with unique sensing capabilities under external stimuli. However, the inherently complex designs and hierarchical architectures seen in nature are difficult to replicate using current fabrication methods.[1] Recent progress in additive manufacturing (AM) technologies has shown to greatly ease these developmental challenges because of their capability to manufacture fully functional devices with complex geometrical morphologies inspired by nature.[1] For example, a maskless lithography 3D printing approach was utilized to fabricate high-resolution structural color patterns inspired by periodic nanostructures seen in peacocks and butterflies.[8] Different structural colors were achieved through magnetic field manipulation of the nanostructures followed by permanently fixing the photonic crystals in a polymer matrix through photopolymerization using projected mask images.[8] Similarly, bioinspired 3D

Received: February 23, 2022
Accepted: March 16, 2022
Published: March 24, 2022

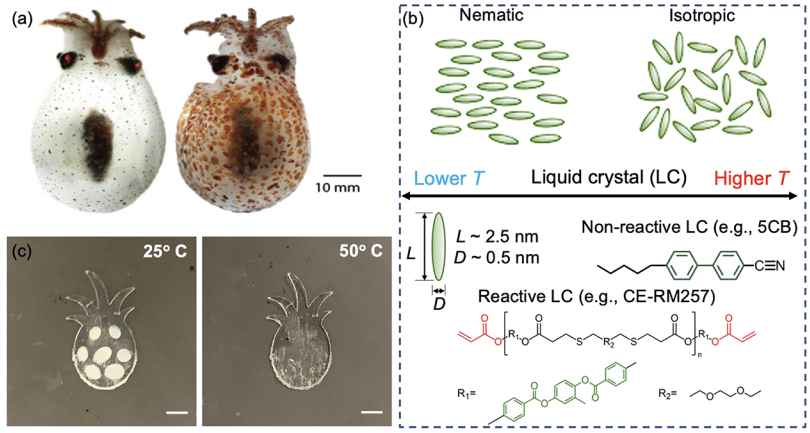

Figure 1. Smart optical materials fabricated using a thermotropic LC mixture. (a) Appearance changes of the *Japetella heathi* octopus under external stimuli. (b) Design of smart optical materials using (non) reactive liquid crystals that exhibit a change in transparency near the nematic-to-isotropic transition temperature and (c) appearance changes of the MVPP-printed artificial octopus under a temperature change. Adapted with permission from ref 5. Copyright 2011 Elsevier.

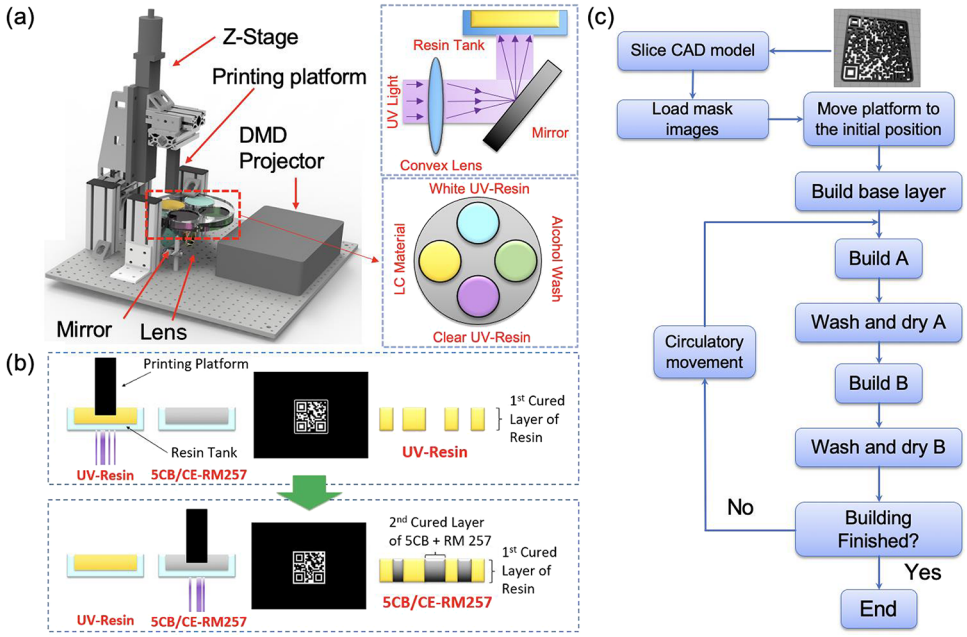

Figure 2. Schematic diagram of the MVPP-based 3D printing platform for the fabrication of smart optical materials. (a) Schematic diagram of the prototype machine of MVPP, (b) multimaterial printing process planning showing the formation of a single layer composed of photocurable acrylic resin and the LC material, and (c) flowchart of the MVPP process to fabricate the multimaterial functional optical part using photocurable acrylic resin and the LC material.

artificial eye structures with a highly efficient array of hexagonal shapes were produced using nanoscale laser writing-based 3D printing to achieve a distortion-free wide field of view, large numerical aperture, and low surface roughness.[9] This work demonstrates that recent advancements in AM technologies can be an attractive tool in order to fabricate functional optical devices with biomimetic materials and structures.[10] Furthermore, this can be further expanded upon for the design of future smart materials for various applications that were previously unachievable through conventional fabrication methods.[11]

Smart devices have gained increased attention due to their numerous applications for wearable sensors,[12] smart windows,[13] and display devices.[14] Emerging smart materials facilitate modifications of microstructures and consequently changes of properties exhibited by the material under a variety of external stimuli.[15] For example, modulation of mechanical stress was demonstrated to control light transmission and structural colors of composite films by tuning periodic microstructures.[16] However, conventional manufacturing methods such as milling or casting have significant limitations in the fabrication of smart optical materials where complex designs and unique configurations are often costly and difficult to achieve.[1] Rising AM technologies have become feasible approaches in developing smart optical materials that can incorporate highly accurate controlled distribution of transparent and opaque materials for use in detectors.[15] Additionally, self-assembly methods containing materials such as copolymers, colloids, and liquid crystals (LCs) to create microstructures with tunable optical properties provide a vast source of unique material systems for AM approaches to develop smart optical devices.[17] Integration of LCs with the

https://doi.org/10.1021/acsapm.2c00322
ACS Appl. Polym. Mater. 2022, 4, 2951−2959

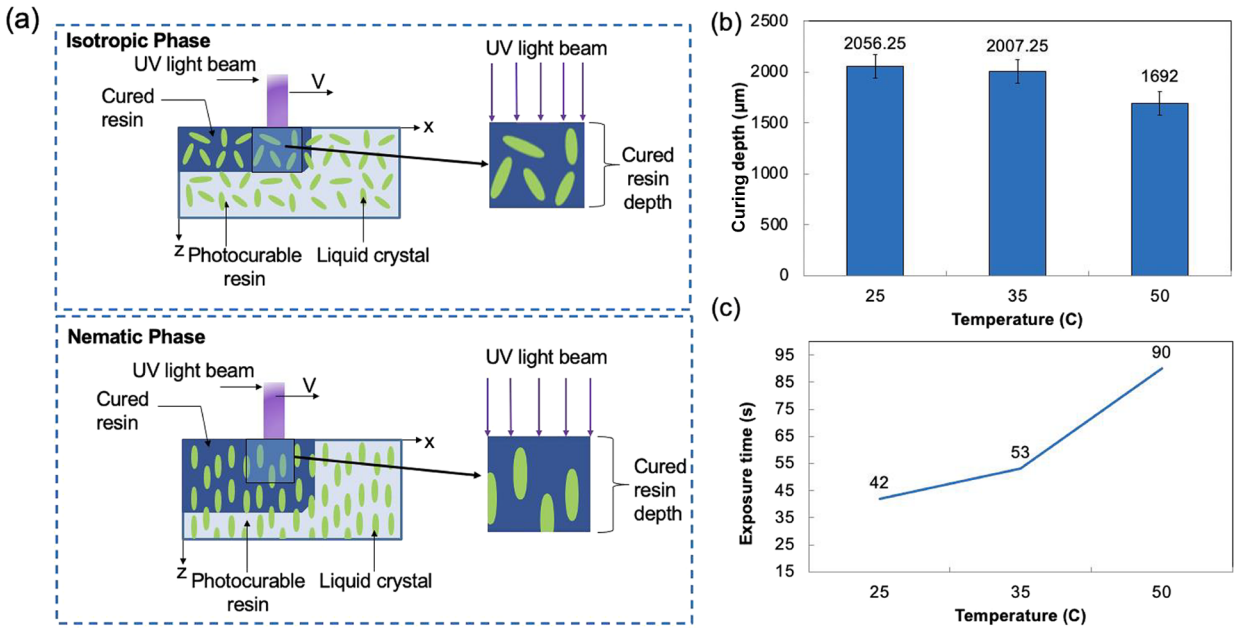

Figure 3. Curing characterization of nematic and isotropic LCs. (a) Effect of isotropic and nematic phases of thermotropic LCs on the light penetration of the exposed light beam and curing depth (b) and exposure time (c) characterization of thermotropic LCs at different temperatures ranging from 25 to 50 °C.

advanced 3D printing process could potentially lead to the fabrications of smart materials with sensing capabilities due to the nematic and isotropic phase transitions of LCs.[18−20] As shown in Figure 1b, thermotropic LCs, such as 4-cyano-4′-pentylbiphenyl (5CB) and chain-extended RM257 (CE-RM257), have a unique and prolate rodlike structure that reversibly changes its bulk spatial orientation when modulating the local temperature of the molecules. When brought below the nematic-to-isotropic transition temperature,[21] the LCs can transition from a randomly oriented state in the isotropic phase to an aligned state in the nematic phase, resulting in a switch from a transparent appearance to an opaque appearance. When LCs are brought above the nematic-to-isotropic transition temperature,[21] the LCs will lose orientation order and recover the transparency. However, there is not much research on fabrication of smart optical devices using AM techniques with LC-based multimaterials with a tunable transparent appearance under the influence of thermal or electric fields.[20]

We would to achieve materials that are capable of changing their transparency in response to external thermal stimuli. The presented research aims to fabricate *Japetella heathi*-inspired smart optical materials through multimaterial vat photopolymerization (MVPP). The nematic and isotropic phases of 5CB and CE-RM257 in a photocurable matrix are initiated through control of the local temperature of cured films fabricated during the photopolymerization. Based on the results from this study, it was demonstrated that the MVPP approach can be used to fabricate smart optical materials with complex design geometries and functionalities that show promise for potential optical applications in various fields. Moreover, the proposed research will help facilitate a better understanding of how to manipulate the orientation of LCs for designing functional devices with enhanced thermal, electrical, and optical performance.

2. RESULTS AND DISCUSSION

2.1. Multimaterial 3D Printing of Functional Optical Materials. An LC-based material consisting of a nonreactive mesogen (5CB), reactive mesogens (i.e., chain-extended RM257 and CE-RM257), and photoinitiators was prepared for vat photopolymerization. Neat RM257 was chain-extended using dithiol to form CE-RM257 oligomers, which can further be readily cross-linked to form a network of polymer chains in the presence of ultraviolet (UV) light of 405 nm wavelength. As illustrated in Figure 2a, the MVPP process was used to selectively cure a conventional acrylic-based UV resin and an LC-based photocurable material in a layer-by-layer manner to form high-resolution geometries and complex 3D shapes. The interface between two different photocurable materials is robust, and the bonding of two materials can be further improved by designing the intertwined infills in the interface.[22] The viscosities of LC-based materials were evaluated through rheological measurements at different concentrations of 5CB and CE-RM257 (Figure S1 in the Supporting Information). Experimental results show that pure CE-RM257 is a highly viscous reactive mesogen that exhibits non-Newtonian fluid behavior. Pure CE-RM257 was diluted using the nonreactive mesogen, i.e., 5CB, to achieve the modification of the phase transition temperature. A mixture of 80% (w/w) 5CB and 20% (w/w) CE-RM257, namely, the 80/20% 5CB/CE-RM257 mixture, was identified as the most optimal composition to fabricate 3D printed thermal sensing devices compared to 50/50% 5CB/CE-RM257 and neat CE-RM257 because of the viscosity. To avoid leakage of nonreactive 5CB and make the printed objects stable, a layer of robust UV photocurable acrylic-based resin was printed around the LCs so that the nonactive 5CB can be encapsulated inside the printed acrylic-based photocurable polymer.

With the purpose of fabricating a thermal sensing quick response (QR) code using the MVPP process, a set of mask images were generated by slicing the digital model, and each pixel of sliced images was marked with the material index

https://doi.org/10.1021/acsapm.2c00322
ACS Appl. Polym. Mater. 2022, 4, 2951−2959

corresponding to the two photosensitive materials (LCs and acrylic resin) (Figure 2b). 2D light beams were further formed by a digital mirror device (DMD), and the focused 2D patterned light beam was exposed onto the surface of the resin. The first and last layer of the QR code was fabricated by curing the acrylic-based UV resin to seal the nonreactive 5CB. A layer thickness of 200 μm and an exposure time of 1.5 s were used for the fabrication of each layer. The printing platform was moved upward after one layer's fabrication, and the newly solidified layer was washed thoroughly with alcohol to remove any residual uncured material before switching the resin tank containing the remaining material. To fabricate the LCs and acrylic resins in the same layer, the printing platform was lowered to the same thickness from the previous layers forcing the new material to permeate the remaining uncured areas where different types of materials were designed. The LCs were printed at room temperature in the nematic phase, and the exposure time and layer thickness were set based on the study of the curing characterization of LCs. The multimaterial printing process is automated, and various types of multimaterial sensing devices with flexible design of material distributions can be fabricated into a single functional component using the MVPP process.[23] The flowchart of the MVPP process to fabricate the multimaterial functional optical part using photocurable acrylic resin and the LC material is shown in Figure 2c.

2.2. Investigation of Curing Characteristics. The curing characteristics of the photosensitive LC material at different phase states were studied. The curing characteristics of the LC material and the printing resolution of MVPP were heavily influenced by the spatial orientation and the phase state of the LCs. As shown in Figure 3a, when a 2D patterned light beam is projected on LCs in the nematic phase, the nematic director is aligned parallel to the projection direction of the incident light beam so that the tightly packed LCs allow the light beam to penetrate the material. In terms of LCs in the isotropic phase, the randomly directed LCs scatter the 2D patterned light beam, leading to the reduction of the light penetration. Consequently, LCs in the nematic phase promote the photopolymerization process and subsequently affect the energy penetration depth of the projected UV light beam since the mean number of pathways in which photons can penetrate the photocurable material becomes significantly increased.[22] For LCs in different phases and molecular orientations, the exposure time of the projected 2D patterned light beam must be adjusted in order to promote photopolymerization of the reactive mesogen to produce LCs with a desired geometry.

Curing depths of the thermotropic LCs in the nematic and isotropic phases were characterized and studied for the fabrication of smart optical components using MVPP. The nematic phase of LCs, of which the molecular orientations are parallel to the projection direction at room temperature, allows the UV light beam to facilitate the photopolymerization process of LCs more easily when compared to LCs in the isotropic phase. The formation of closely arranged calamitic molecules, with bulk alignment perpendicular to the 2D light pattern in the isotropic phase, will increase light scattering due to agglomerations of LC domains that are directly adjacent to one another. A relationship between light penetration and energy distribution was used to formulate an accurate expression for determining the curing depth of the photosensitive LCs. The curing model of thermotropic LCs in the MVPP process can be determined through the basic working curve by Jacobs, using the following equation:[24,25]

$$C_d = D_p \ln\left(\frac{E_0}{E_{cr}}\right) \quad (1)$$

where D_p is the penetration depth in the LC mixture at which the light intensity decreases to $1/e$ of the light intensity at the surface, E_0 is the energy received by the LC mixture, and E_{cr} is the critical energy necessary to initiate photopolymerization of the LC mixture.

The curing depth characteristics of LCs were evaluated at different temperatures to compare characteristics associated with the nematic and isotropic phases. As shown in Figure 3b, the curing depth significantly decreased as the temperature of the photosensitive LC mixture passed the nematic−isotropic transition temperature. For example, when the local temperature of the photosensitive LCs was increased to 50 °C, the curing depth C_d of the photosensitive LC mixture drastically decreased from 2 (nematic phase) to 1.7 mm (isotropic phase). Moreover, as the temperature of the photosensitive LC mixture was further increased, the curing depth remained nearly constant before reaching the transition temperature since the LCs remained vertically oriented. The exposure times of the photosensitive LC mixtures at nematic and isotropic phases, which were cured at different temperatures, are shown in Figure 3c. It was observed that when the 2D light patterns were projected with a constant light intensity, increased exposure times were required to cure a single layer of the photosensitive LC mixture near the isotropic phase compared to the nematic phase to achieve the fabrication of materials with the same desired geometry. For example, an exposure time of 42 s was required to adequately cure the photosensitive LC mixture at 25 °C (nematic phase), while 90 s was needed for curing the photosensitive LC mixture at 50 °C (isotropic phase). A similar tendency was observed when compared to the curing depth of the photosensitive LC mixture. Exposure times of the photosensitive LC mixture at temperatures preceding the nematic−isotropic transition temperature only increased from 42 s in the nematic phase at 25 °C to approximately 53 s at the nematic−isotropic phase change temperature of 39 °C. The exposure times were set to fabricate multimaterial 3D objects with a precise spatial resolution and accurate dimensions during the MVPP process, and the layer thickness was set to 2/3 of the curing depth of the photosensitive LC mixture to achieve smooth surface quality.[24] The cross-linking ratio of the photosensitive LC mixture is determined by the exposure time and light intensity of the projected 2D light beam. The mechanical properties of the printed LCs can be further modulated by adjusting the cross-linking ratio of the photosensitive LC mixture during the printing of MVPP.[26−28]

2.3. Investigation of Shape Changing. The shape changing properties of MVPP-printed thermotropic LCs were investigated at different temperatures. The thermotropic LCs are composed of molecules with rigid, rodlike structures that can align at room temperature in the nematic phase. Upon heating, LCs will adopt a random molecular alignment and show isotropic properties at higher temperatures. Anisotropic alignment of these molecules in the nematic phase results in an anisotropic functional property, which is determined by the nematic director. After extracting the unreacted 5CB, the aligned LC film was generated since the LCs were printed in

https://doi.org/10.1021/acsapm.2c00322
ACS Appl. Polym. Mater. 2022, 4, 2951−2959

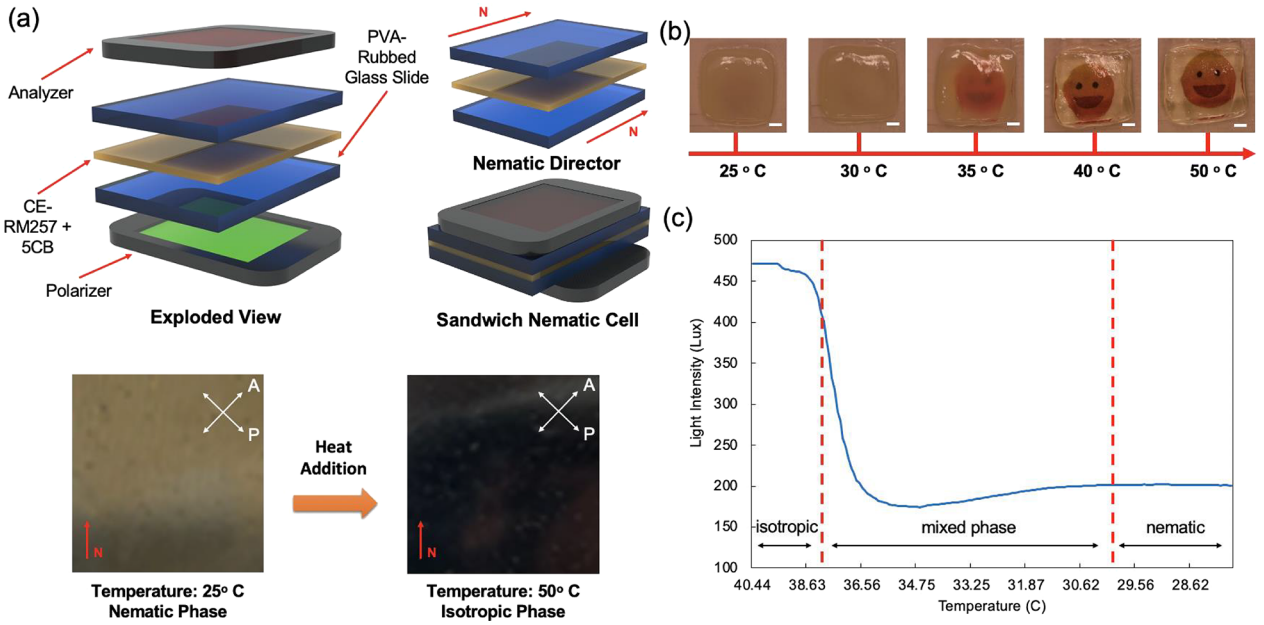

Figure 4. Optical transmission and phase changing properties of MVPP-printed LC films. (a) Verification of LC phase change using cross-polarized microscopy and a nematic director determined by the direction of PVA channels; (b) transparency of the 3D printed LC film under different temperatures, all scale bars are 1 mm; (c) optical transmission curve of the 3D printed LC film that went through isotropic, mixed, and nematic phases during the cooling process.

the nematic phase at room temperature. Due to the alignment, the shape changing of LCs after removing the unreacted 5CB showed anisotropy, and the LC film shrank more in the parallel direction than the one perpendicular to the alignment.[29] We further studied the shape changing of MVPP-printed LC films under different temperatures. Dimensions of MVPP-printed LC films at temperatures ranging from 25 to 50 °C were measured to identify their shape changing property. The shrinkage percentages of the MVPP-printed LC films throughout all tested temperatures are shown in Figure S3. The MVPP-printed LCs shrank more with increasing of temperatures. After heating the MVPP-printed LCs, the shrinkage percentages became bigger in the parallel direction than the one perpendicular to the nematic director and the orientation of the LCs at room temperature.

2.4. Investigation of Thermosensitivity. Previous experiments investigating the molecular thermodynamic behavior close to the nematic-to-isotropic phase transition temperature in LCs have been established using the Landau–de Gennes mean field theory.[29,30] In general, the phase changing properties of thermotropic LCs near the nematic-to-isotropic phase transition temperature were weakly of the first order and dependent on fluctuations of the order parameter due to the free energy density of the system.[31,32] Thermotropic LCs that are heated above the nematic–isotropic transition temperature will readily transition from a low-temperature uniaxial nematic phase to a high-temperature isotropic phase where the orientation of LC molecules is random with respect to each other. Therefore, the phase changing properties of thermotropic LCs were confirmed using cross-polarized microscopy and rubbed polyvinyl alcohol (PVA) channels, to define the nematic director and the orientation of the LCs, through variations in the molecular order of the LC mixture.

As shown in Figure 4a, the phase change of the LCs was monitored using two crossed polarizers positioned ±45° from the nematic director defined by the direction of the rubbed PVA channels. In this orientation, the nematic cell configuration allowed for the full transmission of polarized light when the local temperature of LCs was at room temperature (25 °C). However, when the LCs were heated to 50 °C,they failed to induce a plane change of incoming polarized light compared to the nematic phase and were subsequently blocked by the analyzer where no light transmission was observed. The light transmission during the cooling process of the nematic cell gradually changed to full intensity as the LCs reversed their phase from isotropic to nematic (see Video S1 in the Supporting Information). Therefore, the experimental results confirm the transition of the synthesized LC solution from the nematic to the isotropic phase between 25 and 50 °C.

Optical transmission due to the phase change of the 3D printed LC film for a range of temperatures is shown in Figure 4b. A 3D printed LC film, fabricated by the MVPP process, was initially opaque at room temperature (25 °C). Once the 3D printed film was heated, the 3D printed LC film transitioned from opaque to fully transparent when the temperature was higher than 40 °C, and the hidden image underneath the film became increasingly more visible. Furthermore, DSC results (Figure S4) validated our experimental results with a measured nematic-to-isotropic transition temperature of the uncured 80/20% 5CB/CE-RM257 material of ∼39 °C. Additionally, experimental results from thermogravimetric analysis (TGA) indicated that the 3D printed LC film exhibited good thermal stability within the tested temperature range where material decomposition can be seen at approximately 192 °C (Figure S4). Similar to the results obtained from the phase transition of LCs, the 3D printed LC film dissipated heat gradually over time and eventually reverted to the initial opaque form. The observation of the transparency changes in the local area exhibited a homogeneous change with the temperature of the local area at the same level (see Video S2 in the Supporting Information).

https://doi.org/10.1021/acsapm.2c00322
ACS Appl. Polym. Mater. 2022, 4, 2951−2959

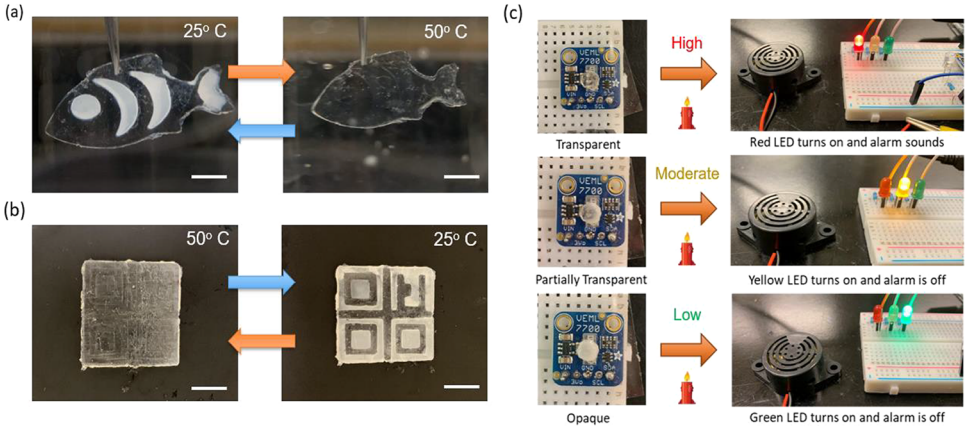

Figure 5. Applications of MVPP-printed LC-based devices with sensing capability. (a) An artificial fish adjusted its appearance along with changing of temperature, (b) the QR code pattern changes in visibility and alters its appearance when the temperature varied, and (c) the LC-based temperature sensor alarmed when the local temperature was above the safety threshold; all scale bars are 2 mm.

In addition, light transmission of 3D printed LC films at different LC phases was investigated. As shown in Figure 4c, LC films exhibited a high optical transmission, around 475 lux, in the isotropic phase as opposed to the mixed isotropic/nematic phase regions in which the light intensity decreased drastically to approximately 200 lux. This reduction in the light intensity appeared when the overall temperature of the LC film reached the nematic-to-isotropic transition temperature (~39 °C) before reaching a steady light intensity reading at around ~25 °C. More importantly, our results indicate that optical transmission of 3D printing LC films can be controlled by simply modulating the concentration of CE-RM257 in the LC mixture to achieve adjustable thermal sensitivity. Specifically, this variation in the reactive mesogen concentration either results in a reduction or an increase in the phase transition temperature of LCs. Experimental DSC results (Figure S5) showed that neat CE-RM257 has a nematic-to-isotropic transition temperature of 73.6 °C compared to 39.0 °C for the 80/20% 5CB/CE-RM257. Therefore, different percentage weight concentrations of CE-RM257 and 5CB can be utilized to synthesize LC materials for 3D printing of thermal sensors with customizable nematic-to-isotropic transition temperatures by evaluating their optical transmission properties under different temperatures.

2.5. Applications of Bioinspired 3D Printed Optical Materials. Thermotropic LC-based smart devices, including an artificial fish, a QR code, and a temperature sensor, were fabricated through the MVPP process to demonstrate the potential applications (Figure 5). All parts were 3D printed using our developed LC printing solution in the nematic phase at room temperature. As shown in Figure 5a, an artificial fish with the capability to sense the temperature change was printed using multimaterial solutions consisted of acrylic resin and thermotropic LCs solution. The transparency of its eyes, inner ribs, and tail can be reversibly changed according to the local temperature (see Video S3 in the Supporting Information). As the temperature of the surrounding water is increased beyond 39 °C, which is the nematic-to-isotropic phase transition temperature, the inner portions of the fish, composed of the LC-based photocurable material, will alter its appearance from opaque to transparent within 1 s, matching the completely transparent body to hide itself inside the water. Moreover, the developed material and printing process can be used to fabricate anticounterfeiting labels. For example, the MVPP-printed QR code can only be read with scanning devices at a desired temperature, which is related to the nematic-to-isotropic threshold temperature of the LC mixture. The sensing capability of the MVPP-printed QR code can be referred to Video S3 in the Supporting Information.

Based on the thermal sensitivity, the MVPP-printed LC film can be further developed into a temperature sensor based on previously obtained results of optical transmission at different temperatures. As shown in Figure 5c, the MVPP-printed temperature sensor was connected with an integrated circuit consisting of a light intensity sensor with LEDs and buzzer indicators. When the temperature of ambient air changed, the LEDs and the alarm indicated to the user whether the temperature was high, moderate, or low. To be specific, when the environmental temperature was low (25 °C), the LED indicators displayed green light with no audible alarm. When the LC film was at a moderate temperature, which was set at a little bit smaller value than the phase transition temperature of the 3D printed LCs sensor, yellow warning light was displayed with no audible alarm. This is a direct result of the variable transparency and optical transmission of the LC film at low and moderate temperatures where the LC film appeared opaque and partially opaque, respectively. When the temperature was beyond the safe threshold, the sensor became fully transparent and the LED turned red with an audible noise produced from the alarm to indicate to the users the dangerous situation. These experimental results demonstrate the numerous benefits of the MVPP process, which enables increased flexibility when designing and fabricating soft robotics, anticounterfeiting devices, and flexible temperature sensors with complex shapes and intricate geometries.

3. CONCLUSIONS

In this work, we present a route to fabricate smart materials with sensing capabilities and customizable geometries through an MVPP-based 3D printing approach. Synthesis of a nonreactive and reactive mesogen LC mixture, with predefined concentrations, shows the flexibility of our methodology in controlling nematic-to-isotropic transition temperatures, which inherently determines the optical transmission properties of 3D printed structures. In addition, the MVPP process allows for a high level of command over spatial geometries with temperature-responsive architectures for the development of next-generation functional smart devices. The present work

https://doi.org/10.1021/acsapm.2c00322
ACS Appl. Polym. Mater. 2022, 4, 2951−2959

enables the development of smart materials with tunable, thermally responsive characteristics, and the MVPP provides a manufacturing tool for prospective applications of smart materials, such as flexible temperature sensors, anticounterfeiting devices, and soft robotics.

4. METHODS AND MATERIALS

4.1. Preparation of Liquid Crystal-Based Materials. The CE-RM257 synthesis procedure was based on a previous work by Wang *et al.*[33] CE-RM257 was prepared via a thiol-acrylate Michael addition reaction at room temperature between the reactive LC 2-methyl-1,4-phenylene bis(4-(3-(acryloyloxy)propoxy)benzoate) (RM257; LC diacrylate) and chain-extended 2,2′-(ethylenedioxy)diethanethiol (EDDET; dithiol). RM257 (8.409 g, 14.3 mmol) was dissolved in 20 mL of dichloromethane, and the resulting solution was placed into a reactor. The catalyst dipropylamine (0.103 g, 1 mmol) was dissolved in 10 mL of dichloromethane and added dropwise into the reactor. Similarly, EDDET (2.303 g, 12.63 mmol) was dissolved into 10 mL of dichloromethane and added dropwise into the reactor. The resulting mixture was left to stir overnight before air blowing at room temperature overnight in a fume hood and drying at 85 °C in a vacuum oven for 24 h to completely remove the solvent.[34]

In a typical preparation of a 3D printing mixture, the reactive CE-RM257 (1.28 g) and nonreactive 5CB (4.8 g) mesogens were separately dissolved in 5 mL of dichloromethane and then combined into one solution to which a photoinitiator (Omnirad 2100, 5 wt % relative to CE-RM257, i.e., 0.064 g) was added. The solvent was removed by air blowing and then vacuum drying overnight at room temperature, resulting in a 79.2/19.8/1.0 wt % 5CB/CE-RM257/photoinitiator, namely, the 80/20% 5CB/CE-RM257 3D printing formulation.

4.2. Curing Characteristics. The curing characteristics of the synthesized LC material were studied at different temperatures to determine the influence of LC phases during the 3D printing process. The LC material was uniformly heated in a resin tank using a hot plate to modulate the local temperature of the material ensuring a homogeneous distribution. An infrared temperature sensor was used to measure the temperature of the LC material within the resin tank before curing. A thin layer of the LC material was selectively cured using a 405 nm wavelength 2D patterned light beam formed by a reflected image from a DMD, which had a 1920 × 1080 array of micromirrors, and focused by a convex lens (purchased from Thorlabs, Inc.) with a focus distance f of 150 mm.[35,36] The curing depth of the resultant film of LCs was quantified by using micrometer high-accuracy calipers (purchased from RexBiTi), while the parameter for exposure time was confirmed by comparing the shape, length, and width of the cured LC film to the desired geometry.

4.3. Optical Transmission Testing and Thermal and Homogeneous Evaluation. Optical transmission properties of MVPP-printed LC films were evaluated at different temperatures using an ambient light source, a light intensity sensor (Adafruit VEML7700 lux sensor), and a temperature probe (DS18B20 temperature sensor). The light sensor and the temperature probe were operated through the use of an Arduino Uno (Arduino Uno REV3) controller. A thin layer of 80% (w/w) 5CB, 20% (w/w) chain-extended RM257, and 5% (w/w) photoinitiators with respect to the mass of RM257 was selectively cured into a small film and placed between an ambient light source and a light intensity sensor. Afterward, optical transmission of the printed LC film was quantified by heating the film to 50 °C, above the nematic−isotropic transition temperature, and subsequently measuring changes in light intensity as the film was allowed to cool to 25 °C. Similarly, the heat dissipation and local area transparency of the printed LC films were captured through infrared videography (FLIR ONE Gen 3) and digital microscopy, respectively, after LC films in the isotropic phase transitioned to the nematic phase.

4.4. Shape Changing Evaluation. Shape changing properties of the MVPP-printed LC films were investigated at different temperatures (refer to Section 2.2). First, a specimen with a 1:1 length-to-width ratio was uniformly heated on a glass slide to the desired temperature using a hot plate. The temperature of the printed LC film was then confirmed using an infrared temperature sensor before subsequent measurements of the width and length were taken using a digital caliper (purchased from EAGems). The shrinkage percentage was then calculated for comparison using measurements of the width and length, at a specific temperature of LC films, using the following equation:

$$A_{=} = \frac{L_t}{L_r} \tag{2}$$

$$A_{\perp} = \frac{W_t}{W_r} \tag{3}$$

where the shrinkage percentages of LCs in the directions parallel and perpendicular to the nematic director and the orientation of the LCs at room temperature are $A_{=}$ and $A_{\perp}$, respectively; L_t and W_t are the length and the width of the LC film at temperature t, respectively; L_r and W_r are the length and the width of the LC film at room temperature (25 °C), respectively.

4.5. TGA and Viscosity Measurements. The rheological measurements were conducted on a Discovery HR 30 rheometer at room temperature. Steady-state shear rate sweep tests were performed to analyze the rheological behavior of the LC mixtures and neat 5CB with relatively low viscosities, whereas an oscillation frequency sweep was conducted on the neat CE-RM257 with a relatively high viscosity. The Cox−Merz rule was applied to the neat CE-RM257 sample to convert the obtained complex viscosity vs angular frequency data into viscosity vs shear rate data. Figure 4 shows the viscosity vs shear rate for neat CE-RM257, 50/50% 5CB/CE-RM257, 80/20% 5CB/CE-RM257, and neat 5CB samples. Thermogravimetric analysis (TGA) measurements were conducted on a TGA 5500 at 700 °C using a heating rate of 10 °C/min under a nitrogen atmosphere. The onset decomposition temperature corresponding to a 10% weight loss of the sample was determined to be 206 °C.

■ ASSOCIATED CONTENT

Supporting Information

The Supporting Information is available free of charge at https://pubs.acs.org/doi/10.1021/acsapm.2c00322.

Additional analytical results including DSC, TGA, rheology, NMR, shape changing, and optical transmission results (PDF)

Visualization of the LC phase change using cross-polarized microscopy and a nematic director determined by the direction of PVA channels (MP4)

IR and light microscopy video showing the thermal and transparency distribution of a 3D printed LC film when the temperature cooled down from 50 °C to room temperature (25 °C) (MP4)

Artificial fish and QR code under different temperatures (MP4)

■ AUTHOR INFORMATION

Corresponding Authors

Kailong Jin − *Department of Chemical Engineering and Biodesign Center for Sustainable Macromolecular Materials and Manufacturing, Arizona State University, Tempe, Arizona 85287, United States;* orcid.org/0000-0001-5428-3227; Email: kailong.jin@asu.edu

Xiangjia Li − *Department of Mechanical and Aerospace Engineering and Biodesign Center for Sustainable Macromolecular Materials and Manufacturing, Arizona State University, Tempe, Arizona 85287, United States;*

orcid.org/0000-0002-8549-4251; Email: xiangjia.li@asu.edu

Authors

Dylan Joralmon − *Department of Mechanical and Aerospace Engineering, Arizona State University, Tempe, Arizona 85287, United States*

Saleh Alfarhan − *Department of Chemical Engineering, Arizona State University, Tempe, Arizona 85287, United States*

Stephanie Kim − *Department of Mechanical and Aerospace Engineering, Arizona State University, Tempe, Arizona 85287, United States*

Tengteng Tang − *Department of Mechanical and Aerospace Engineering, Arizona State University, Tempe, Arizona 85287, United States*

Complete contact information is available at: https://pubs.acs.org/10.1021/acsapm.2c00322

Author Contributions

D.J., K.J., and X.L. conceived and designed the experiments. S.A. and K.J. prepared the material solution. D.J., S.A., S.K., and T.T. performed experiments, data collection, and analysis. D.J. and S.K. worked on the demonstration applications and video editing. All authors discussed, wrote, and commented on the manuscript.

Notes

The authors declare no competing financial interest.

■ ACKNOWLEDGMENTS

We acknowledge funding support from the ASU startup funding, the ASU FSE Strategic Interest Seed Funding Award, and the National Science Foundation (NSF grant no. CMMI 2114119).

■ REFERENCES

(1) Yang, Y.; Song, X.; Li, X.; Chen, Z.; Zhou, C.; Zhou, Q.; Chen, Y. Recent progress in biomimetic additive manufacturing technology: from materials to functional structures. *Adv. Mater.* **2018**, *30*, 1706539.

(2) Barber, A. H.; Lu, D.; Pugno, N. M. Extreme strength observed in limpet teeth. *J. R. Soc., Interface* **2015**, *12*, 20141326.

(3) Buck, J.; Buck, E. Photic signaling in the firefly Photinus greeni. *Biol. Bull.* **1972**, *142*, 195−205.

(4) Teyssier, J.; Saenko, S. V.; Van Der Marel, D.; Milinkovitch, M. C. Photonic crystals cause active colour change in chameleons. *Nat. Commun.* **2015**, *6*, 6368.

(5) Zylinski, S.; Johnsen, S. Mesopelagic cephalopods switch between transparency and pigmentation to optimize camouflage in the deep. *Curr. Biol.* **2011**, *21*, 1937−1941.

(6) Kim, J. H.; Moon, J. H.; Lee, S. Y.; Park, J. Biologically inspired humidity sensor based on three-dimensional photonic crystals. *Appl. Phys. Lett.* **2010**, *97*, 103701.

(7) Parker, A. R.; Martini, N. Structural colour in animals—simple to complex optics. *Opt. Laser Technol.* **2006**, *38*, 315−322.

(8) Kim, H.; Ge, J.; Kim, J.; Choi, S. E.; Lee, H.; Lee, H.; Park, W.; Yin, Y.; Kwon, S. Structural colour printing using a magnetically tunable and lithographically fixable photonic crystal. *Nat. Photonics* **2009**, *3*, 534−540.

(9) Wu, D.; Wang, J. N.; Niu, L. G.; Zhang, X. L.; Wu, S. Z.; Chen, Q. D.; Lee, L. P.; Sun, H. B. Bioinspired Fabrication of High-Quality 3D Artificial Compound Eyes by Voxel-Modulation Femtosecond Laser Writing for Distortion-Free Wide-Field-of-View Imaging. *Adv. Opt. Mater.* **2014**, *2*, 751−758.

(10) Zhu, Y.; Tang, T.; Zhao, S.; Joralmon, D.; Poit, Z.; Ahire, B.; Li, X. Recent Advancements and Applications in 3D Printing of Functional Optics. *Addit. Manuf.* **2022**, No. 102682.

(11) Zhu, Y.; Joralmon, D.; Shan, W.; Chen, Y.; Rong, J.; Zhao, H.; Li, X. 3D printing biomimetic materials and structures for biomedical applications. *Bio-Des. Manuf.* **2021**, *4*, 405−428.

(12) Tzou, H. S.; Lee, H. J.; Arnold, S. M. Smart materials, precision sensors/actuators, smart structures, and structronic systems. *Mech. Adv. Mater. Struct.* **2004**, *11*, 367−393.

(13) Sun, X. W.; Wang, Z. H.; Li, Y. J.; Yang, H. L.; Gong, G. F.; Zhang, Y. M.; Yao, H.; Wei, T. B.; Lin, Q. Transparency and AIE tunable supramolecular polymer hydrogel acts as TEA−HCl vapor controlled smart optical material. *Soft Matter* **2020**, *16*, 5734−5739.

(14) Mandel, K.; Granath, T.; Wehner, T.; Rey, M.; Stracke, W.; Vogel, N.; Sextl, G.; Müller-Buschbaum, K. Smart Optical Composite Materials: Dispersions of Metal−Organic Framework@ Superparamagnetic Microrods for Switchable Isotropic−Anisotropic Optical Properties. *ACS Nano* **2017**, *11*, 779−787.

(15) Carrasco-Correa, E. J.; Simó-Alfonso, E. F.; Herrero-Martínez, J. M.; Miró, M. The emerging role of 3D printing in the fabrication of detection systems. *TrAC, Trends Anal. Chem.* **2021**, No. 116177.

(16) Ge, D.; Lee, E.; Yang, L.; Cho, Y.; Li, M.; Gianola, D. S.; Yang, S. A robust smart window: reversibly switching from high transparency to angle-independent structural color display. *Adv. Mater.* **2015**, *27*, 2489−2495.

(17) Cecil, F.; Guijt, R. M.; Henderson, A. D.; Macka, M.; Breadmore, M. C. One step multi-material 3D printing for the fabrication of a photometric detector flow cell. *Anal. Chim. Acta* **2020**, *1097*, 127−134.

(18) Dumanli, A. G.; Savin, T. Recent advances in the biomimicry of structural colours. *Chem. Soc. Rev.* **2016**, *45*, 6698−6724.

(19) White, T. J.; Broer, D. J. Programmable and adaptive mechanics with liquid crystal polymer networks and elastomers. *Nat. Mater.* **2015**, *14*, 1087−1098.

(20) Nocentini, S.; Martella, D.; Parmeggiani, C.; Wiersma, D. S. 3D printed photoresponsive materials for photonics. *Adv. Opt. Mater.* **2019**, *7*, 1900156.

(21) Choi, S. H.; Duzik, A. J.; Kim, H. J.; Park, Y.; Kim, J.; Ko, H. U.; Kim, H. C.; Yun, S.; Kyung, K. U. Perspective and potential of smart optical materials. *Smart Mater. Struct.* **2017**, *26*, No. 093001.

(22) Mustafa, I.; Kwok, T. H. Development of Intertwined Infills to Improve Multi-Material Interfacial Bond Strength. *J. Manuf. Sci. Eng.* **2022**, *144*, No. 031009.

(23) Li, X.; Yang, Y.; Xie, B.; Chu, M.; Sun, H.; Hao, S.; Chen, Y.; Chen, Y. 3D printing of flexible liquid sensor based on swelling behavior of hydrogel with carbon nanotubes. *Adv. Mater. Technol.* **2019**, *4*, 1800476.

(24) Jacobs, P. F. Rapid prototyping & manufacturing: fundamentals of stereolithography. *Soc. Manuf. Eng.* **1992**, 62−100.

(25) Bennett, J. Measuring UV curing parameters of commercial photopolymers used in additive manufacturing. *Addit. Manuf.* **2017**, *18*, 203−212.

(26) Rogez, D.; Brömmel, F.; Finkelmann, H.; Martinoty, P. Influence of Swelling on the Shear Mechanical Properties of Monodomain Side-Chain Liquid-Crystal Elastomers: Gaussian Versus Non-Gaussian Elasticity. *Macromol. Chem. Phys.* **2011**, *212*, 2667−2673.

(27) Yamamoto, T.; Yoshida, M. Viscoelastic and photoresponsive properties of microparticle/liquid-crystal composite gels: tunable mechanical strength along with rapid-recovery nature and photochemical surface healing using an azobenzene dopant. *Langmuir* **2012**, *28*, 8463−8469.

(28) Meeker, S. P.; Poon, W. C. K.; Crain, J.; Terentjev, E. M. Colloid−liquid-crystal composites: An unusual soft solid. *Phys. Rev. E* **2000**, *61*, No. R6083.

(29) Karausta, A.; Bukusoglu, E. Liquid crystal-templated synthesis of mesoporous membranes with predetermined pore alignment. *ACS Appl. Mater. Interfaces* **2018**, *10*, 33484−33492.

(30) de Gennes, P.G.; Prost, J., . *The physics of liquid crystals* (No. *83*). Oxford university press, 1993.
(31) Wiant, D.; Stojadinovic, S.; Neupane, K.; Sharma, S.; Fodor-Csorba, K.; Jakli, A.; Gleeson, J. T.; Sprunt, S. Critical behavior at the isotropic-to-nematic phase transition in a bent-core liquid crystal. *Phys. Rev. E* **2006**, *73*, No. 030703.
(32) Gramsbergen, E. F.; Longa, L.; de Jeu, W. H. Landau theory of the nematic-isotropic phase transition. *Phys. Rep.* **1986**, *135*, 195−257.
(33) Wang, Z.; Wang, Z.; Zheng, Y.; He, Q.; Wang, Y.; Cai, S. Three-dimensional printing of functionally graded liquid crystal elastomer. *Sci. Adv.* **2020**, *6*, No. eabc0034.
(34) Hale, P. S.; Shapter, J. G.; Voelcker, N. H.; Ford, M. J.; Waclawik, E. R. Liquid-crystal displays: Fabrication and measurement of a twisted nematic liquid-crystal cell. *J. Chem. Educ.* **2004**, *81*, 854.
(35) Li, X.; Xie, B.; Jin, J.; Chai, Y.; Chen, Y. 3D Printing Temporary Crown and Bridge by Temperature Controlled Mask Image Projection Stereolithography. *Proc. Manuf.* **2018**, *26*, 1023−1033.
(36) Li, X.; Baldacchin, T.; Song, X.; Chen, Y., *Multi-Scale Additive Manufacturing: An Investigation on Building Objects With Macro-, Micro- and Nano-Scales Features*; 11th International Conference on Micro Manufacturing: Irvine, CA,2016 Mar. 29, pp. 96.

https://doi.org/10.1021/acsapm.2c00322
ACS Appl. Polym. Mater. 2022, 4, 2951−2959